

Fabrication of heterojunction $\text{MnTiO}_3\text{-TiO}_2$ -decorated carbon nanofibers via electrospinning as an effective multifunctional photocatalyst

Ayman Yousef^{1,*}, Nasser I. Zouli¹, Ibrahim M. Maafa^{1,†}, Haitham M. Hadidi², Sahar Sallam³, Majed Moosa⁴, M. M. El-Halwany⁵

¹Department of Chemical Engineering, College of Engineering, Jazan University, Jazan 45142, Saudi Arabia

²Department of Mechanical Engineering, College of Engineering, Jazan University, Jazan 45142, Saudi Arabia

³Department of Chemistry, College of Science, Jazan University, Jazan 45142, Saudi Arabia

⁴Department of Industrial Engineering, College of Engineering, Jazan University, Jazan 45142, Saudi Arabia

⁵Engineering Mathematics and Physics Department, Faculty of Engineering, Mansoura University, El-Mansoura, Egypt

In this paper, we successfully synthesized heterojunction manganese titanate/titanate nanoparticles ($\text{MnTiO}_3\text{-TiO}_2$ NPs)-decorated carbon nanofibers (CNFs) employing the electrospinning process. The morphology, crystallinity, and chemical composition of the $\text{MnTiO}_3/\text{TiO}_2$ -decorated CNFs is characterized via SEM, FESEM, STEM, TEM EDX, and XRD techniques. The synthesized nanocomposite exhibits good performance for photodegradation of methylene blue (MB) dye and hydrolysis of ammonia–borane complex for hydrogen releasing experiment in a batch reactor under visible light. A mathematical model was developed to predict the photocatalytic activity of the produced nanocomposite with various parameters. The operational parameters include the effect of the initial concentration, catalyst dosage, light intensity, and reaction temperature, which are studied to validate the mathematical model. The reaction rate constant of MB photodegradation is found to be 0.0153 min^{-1} for an initial MB concentration of $5 \text{ mg}\cdot\text{L}^{-1}$ with a catalytic dosage of $200 \text{ mg}\cdot\text{L}^{-1}$ at a reaction temperature of 25°C under a light intensity of $25 \text{ W}\cdot\text{m}^{-2}$. Similarly, the H_2 generation employing TiO_2 @CNFs and $\text{MnTiO}_3/\text{TiO}_2$ @CNFs under visible light irradiation is observed to be 0.31 mol and 2.95 mol, respectively, corresponding to an exposure of 10 min. We also demonstrated that the yield of hydrogen employing $\text{MnTiO}_3/\text{TiO}_2$ @CNFs under visible light increases to 2.95 mol compared with 1.51 mol in darkness. Finally, comparisons were made between the experimental and model-predicted values of the reaction rate constant and final concentrations. Theoretical and experimental data of photocatalytic activity are found to be in good agreement for $\text{MnTiO}_3/\text{TiO}_2$ @CNFs.

Keywords: *manganese titanate nanoparticles, dye removal, ammonia–borane complex, hydrogen release, electrospinning, visible light*

1. Introduction

Environmental pollution and the energy crisis are considered the major challenges faced by mankind in the 21st century. Approximately 1%–20% of the worldwide dye production from industries is released into water as industrial effluent [1–3]. Industrial effluent—through oxidation, hydrolysis, or other chemical reactions—produces toxic metabolites in wastewater [4–6]. According to the UNESCO World Water Assessment Pro-

gramme (2003), nearly 2 million tons of water per day are discharged from industries and agricultural fields [7]. Due to the limited freshwater availability and rapid population growth, an urgent need is encountered to pay greater attention to the recycling of wastewater effluent. Effective and safe treatment of wastewater incurs exorbitantly high investment. The ecofriendly and economical photocatalyzed water purification process that employs semiconductors has been considered the most suitable process to degrade and mineralize organic water pollutants under ultraviolet (UV) or visible rays. The most common photocatalyst is TiO_2 ,

* E-mail: aymanhassan@jazanu.edu.sa

† E-mail: imoafa@jazanu.edu.sa

which is also used in various types of applications such as self-cleaning coatings, photoelectrochemical (PEC) water splitting, and dye-sensitized solar cells (DSSC) [4, 5]. Due to its wide bandgap (3.0 eV for rutile and 3.2 eV for anatase), it can only absorb light in the UV region. Moreover, it has drawback of rapid recombination of electron-hole pairs [6, 7]. Thus, the photolytic performance of TiO_2 is enhanced through the introduction of metallic and non-metallic ion doping, which expands the light absorption range of titania from UV to the visible range [8].

In recent years, ilmenite has been utilized as an efficient photocatalyst, owing to its ability to degrade organic pollutants when exposed to visible radiation [9–11]. Among them, manganese titanate (MnTiO_3) has attracted the most attention in solar energy applications due to its narrow bandgap (3.1 eV) in the visible region making it suitable for photocatalytic applications [12–14]. He *et al.* [15] reported the synthesis of MnTiO_3 powder and demonstrated its good photocatalytic activity toward aqueous methyl orange at various pH values. Nakhong [7] synthesized MnTiO_3 nanofibers and demonstrated their applicability for utilization in DSSC. Alkaykh *et al.* [16] synthesized MnTiO_3 nanoparticles via sol-gel technique and studied their photocatalytic activity in methylene blue (MB) degradation. The as-prepared photocatalyst possesses high MB degrading ability for heterojunction $\text{MnTiO}_3/\text{TiO}_2$ and MnTiO_3 with the efficiency of 75% and 70%, respectively, under direct sunlight exposure for 240 min. Compared to TiO_2 , MnTiO_3 has a low conduction band (CB) gap that inhibits the recombination rate of electron-hole pairs [17]. Due to certain unique properties of carbon materials such as graphene, interest in the study of carbon nanotubes (CNTs) and carbon nanofibers (CNFs) has recently gained momentum, and accordingly, these are currently used in many applications due to these properties [18, 19]. Moradi *et al.* [20] incorporated FeTiO_3 with graphene oxide (GO) to reduce its bandgap to obtain a further shift toward the visible spectrum. The material was synthesized via an ultrasound-assisted technique and possessed high photocatalytic activity to degrade phenolic compounds when ex-

posed to sunlight for 240 min. They observed that the visible light exhibited faster degradation compared with the UV light. Also, their study concluded that the phenol removal rate was increased with the increased addition of GO to FeTiO_3 . GO acts as a good e^- receiver, which inhibits e^-/h^+ recombination. Moreover, GO improved phenol adsorption by GO/ FeTiO_3 nanocomposite, which ultimately increases the contact of phenol to surface hydroxyl radicals and positive holes. Previous studies have shown that the CNFs have high electrical conductivity with facile capture and transfer of photoinduced charges during the photosynthesis process [21, 22]. Hydrogen is an ecological energy transporter, and is considered to be a clean fuel as compared to petroleum products. However, due to its wide application hydrogen storage in large quantities remains a major challenge. To overcome this issue, hydrogen is stored within solid materials such as boron hydride compounds. Among these compounds, ammonia-borane (AB) complex (NH_3BH_3) carries a sizeable hydrogen content (19.6 wt.%), and is also characterized by high solubility and high stability toward hydrolysis, with a 4-day aqueous solution capacity [23, 24]. Thus, an appropriate channel is vital to liberate hydrogen from AB. Various catalysts have been employed to produce hydrogen from AB. Recently, researchers have focused on the production of hydrogen using the photocatalytic hydrolysis of AB. In this paper, we introduce a heterojunction $\text{MnTiO}_3/\text{TiO}_2$ @CNFs photocatalyst to degrade MB dye and produce hydrogen from the hydrolysis of AB under direct sunlight. The photocatalyst material has been prepared via electrospinning technique, where electrospun nanofiber mats comprised of manganese acetate tetra-hydrate, titanium (IV) isopropoxide, and polyvinylpyrrolidone (PVP) are calcined at a temperature of 900°C. The reaction kinetics and thermodynamics properties are also studied to ascertain the effects of various parameters on the photocatalytic activity.

2. Experimental

2.1. Materials

Titanium isopropoxide (97%), PVP, manganese acetate tetrahydrate (98%), and AB complex (97%) were purchased from Sigma Aldrich (MO 68178, USA). MB (95%) was procured from LobaChemie (mumbai 400 005, India). Ethanol and acetic acid were procured from Scharlau (08181 Sentmenat, BarcelonaSpain).

2.2. Synthesis of MnTiO₃/TiO₂-decorated CNFs

We employed the sol-gel method to synthesize pristine TiO₂-decorated CNFs. Initially, we added 4.4 mmol titanium isopropoxide to 10 wt.% PVP solution. PVP solution was prepared as reported previously in the literature [25–30]. The solution was stirred until it turned into a yellow transparent sol-gel and the formed sol-gel was subjected to the electrospinning process. The positive electrode was connected to a copper pin immersed in sol-gel, and the cathode electrode connected with an aluminum foil covered steel drum. A high voltage of 20 kV magnitude was applied between the electrodes, which were held 15 cm apart. The formed NF mats were then detached from the aluminum foil, kept in a vacuum dryer overnight at 50°C, and then calcined at 900°C for 5 h in an argon atmosphere. The heating rate was maintained at 2.3°C/min. To prepare MnTiO₃/TiO₂-decorated CNFs, we added 4.5 mmol manganese acetate tetrahydrate to the previous solution, with continuous stirring. After obtaining a clear sol-gel, we subjected it to the same aforementioned conditions of electrospinning and calcination processes.

2.3. Characterization

We imaged the surface morphology of the MnTiO₃/TiO₂-decorated CNFs using a JSM-5900 SEM (JEOL Ltd., Tokyo, Japan) operational with energy-dispersive X-ray spectroscopy (EDX). The crystallinity of the NFs was analyzed by the XRD (Rigaku Corporation, Tokyo, Japan) with CuK α ($\lambda = 1.54056 \text{ \AA}$) radiation and 2θ scan in the angular range of 10°–80°. TEM images of high resolution

were obtained using a JEOL JEM-2200FS (TEM) equipped with a 200 kV field emission gun (FEG).

2.4. Determination of MB photodegradation

The photodegradation of MB through the use of MnTiO₃/TiO₂-decorated CNFs was carried out in a simple batch photoreactor consisting of a 150 mL laboratory glass bottle. The light source used in the photocatalytic experiment was a visible fluorescent lamp with a specification of $\lambda = 420\text{--}700 \text{ nm}$ and $I = 23\text{--}40 \text{ W}\cdot\text{m}^{-2}$ (Philips Co., Amsterdam, The Netherlands). Stock solutions from different MB concentrations (5 mg/L, 7.5 mg/L, 10 mg/L, and 15 mg/L) have been prepared. The reactor was charged with a 100 mL aqueous mixture of MB and a predetermined amount of MnTiO₃/TiO₂-decorated CNFs photocatalyst. The solution was kept in darkness to determine the adsorption-desorption of photocatalyst NFs toward MB. Later on, the solution was stirred and exposed directly to visible light. The reaction temperature was controlled by a thermostat water bath. The 3 mL MB solution was withdrawn after specific time intervals of irradiation and solid NFs were separated out from the solution through centrifuging at 3,000 rpm for 5 min. Finally, the absorption of drawn solutions was measured using a UV-visible spectrophotometer (HP8453UV-visible spectroscopy system, Poway, CA, USA).

2.5. Photohydrolysis of AB complex

The photocatalytic activity of MnTiO₃/TiO₂@CNFs toward AB hydrolysis under visible light irradiation was analyzed according to our previous experiment [25]. The same light source that was used in the photodegradation of MB dye was used here also. The reaction mixture, carried in a flask with a Teflon coated magnetic bar, was placed on a magnetic stirrer and associated to a measuring cylinder full of water via a rubber piping to evaluate the volume of the H₂ gas released by the photocatalytic reaction. Then, a mixture of 1 mmol of AB and a predetermined amount of catalyst was added to the reaction flask, and the contents of the flask were exposed to

visible light. The impacts of a range of variables such as AB concentration, catalyst concentration, reaction temperature, and light intensity were studied. The released H₂ gas volume was evaluated by measuring the displacement of the water level.

3. Results and discussion

3.1. Morphology study

Electrospinning is the most common technique to produce excellent nanofibers of inorganic and organic components [30–33]. The calcination of produced electrospun nanofiber mats at high temperatures and inert atmosphere leads to a decrease in the decomposition rate of polymer while keeping the nanofibrous morphology intact [18, 19, 28, 34]. The low magnification (SEM) and high magnification (FESEM) images of electrospun nanofiber mats reveal the presence of MnAc, TIIP, and PVP after vacuum drying at 60°C, with smooth, continuous, and beads-free nanofibrous structure, as shown in Figures 1A and 1B. The NFs preserve a nanofibrous morphology even after the calcination process, as shown in Figures 1C and 1D. However, the size of the nanofibers is reduced, probably due to the partial decomposition of polymer from 245.28 nm (after drying process) to 156.91 nm (after calcination process), as shown in Figures 2A and 2B.

3.2. Phase study

XRD analysis is considered the most reliable technique to analyze the crystal structure of materials. Figure 3 shows the XRD patterns of TiO₂ NFs containing anatase and rutile phases, and the XRD patterns of the synthesized NFs after calcination process. The obtained results reveal the formation of a mixed phase comprising tetragonal TiO₂ rutile phase (JCPDS Card No. 21-1276) and rhombohedral pyrophanite phase MnTiO₃ (JCPDS Card No. 29-0902). Additionally, low intensity peak is observed at 2θ value of 23.1° corresponding to the (002) plane, suggesting the formation of carbon-like graphite because of the partial decomposition of polymer for the duration of the calcination process [35, 36].

TEM EDX has been performed to ascertain the chemical composition of the prepared NFs, as shown in Figure 4. Figure 4A indicates the STEM image of a selected nanofiber, wherein the NF surface is observed to be rough, perhaps due to the escape of gases during the calcination process. EDX analysis of the line in Figure 4A is shown in Figures 4B–4E. It is evident from Figures 4B–4D that Ti, Mn, and O have the same distributions, which confirms the formation of MnTiO₃ and TiO₂. Figure 4D suggests that carbon is the outermost element in the synthesized NFs composite. In other words, MnTiO₃ and TiO₂ composites are covered with carbon. The presence of carbon can enhance the overall photocatalytic process due to enhancement in photoinduced e[−] and h⁺ separation, increased exposure to the photocatalyst, and ease of adsorption process.

3.3. Photocatalytic degradation of MB

To understand the photodegradation of MB dye employing MnTiO₃/TiO₂@CNFs, we examined the effect of the following parameters on the photodegradation process: (i) MB dye concentration (*C_i*), (ii) reaction temperature (*T*), (iii) CNFs dosage, and (iv) light intensity (*I*). The mathematical model employed to evaluate the photocatalytic reaction as a function of operational parameters is as follows [37]:

$$K_{app} = K' \left(\frac{K_R}{1 + K_R C_i} \right) \cdot \left(\frac{K_{NFs} C_{NFs}}{1 + K_{NFs} C_{NFs}} \right) \left(\exp \frac{-E_a}{RT} \right) (mI) \quad (1)$$

Where:

K_{app} – represents the reaction rate constant (expressed in min^{−1}),

K' – the equation constant (mg·L^{−1}),

K_R – the adsorption equilibrium constant (L·mg^{−1}),

E_a – the activation energy (J·mol^{−1}),

R – the universal gas constant (J·K^{−1}·mol^{−1}),

C_i – the initial MB dye concentration (mg·L^{−1}),

T – the reaction temperature (K),

I – the light intensity (W·m^{−2}),

m – the coefficient for light intensity (m²·W^{−1}·min^{−1}),

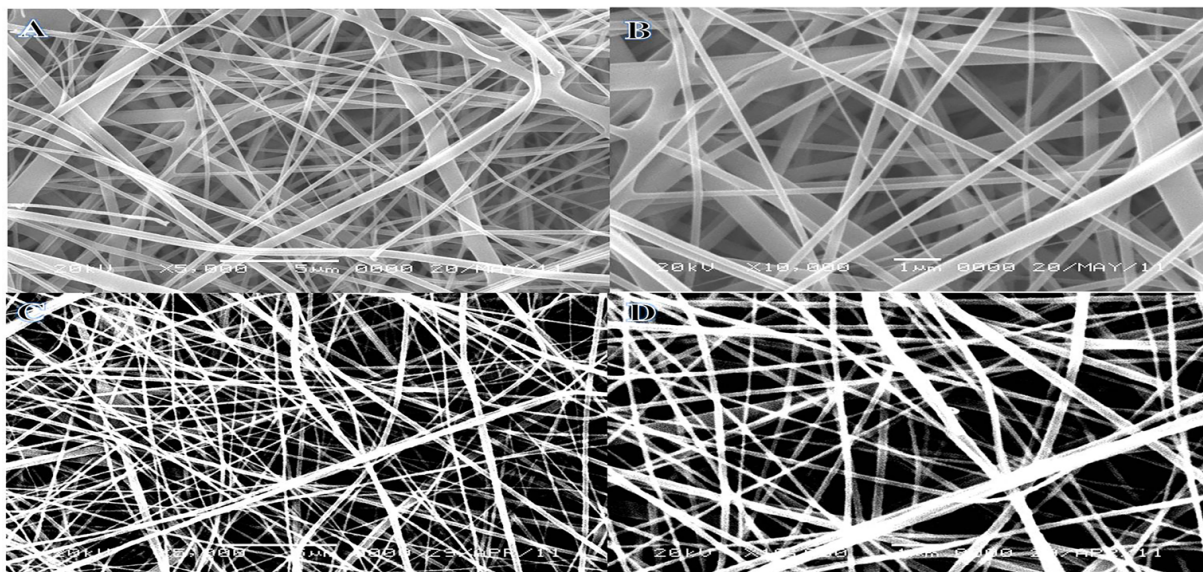


Fig. 1. (A, B) SEM and FESEM images of the electrospun MnAc/TIIP/PVP nanofibers mat after drying at 60°C for 24 h. (C, D) SEM and FESEM images of the calcined nanofibers at 800°C in Ar atmosphere. PVP, polyvinylpyrrolidone

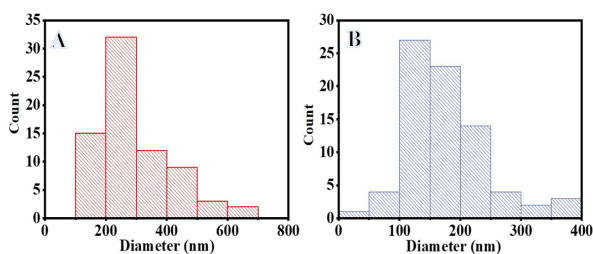


Fig. 2. Size distribution of the nanofibers before calcination (A) and after calcination (B)

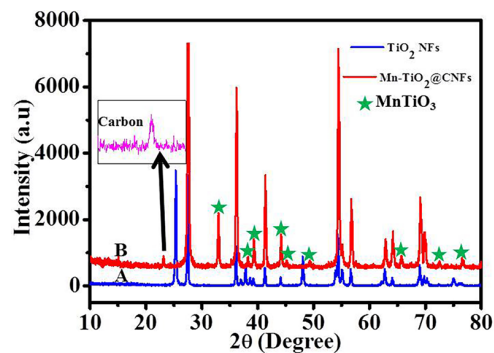


Fig. 3. XRD patterns of the powders obtained from the calcination of MnAc/TIIP/PVP at 800°C in Ar atmosphere. CNFs, carbon nanofibers; PVP, polyvinylpyrrolidone

K_{NFs} – the adsorption constant for catalyst dosage ($L \cdot mg^{-1}$), and C_{NFs} – the catalyst dosage ($mg \cdot L^{-1}$).

Figure 5 shows the change of MB concentration vs. irradiation time in the absence of photocatalyst NFs, and with $TiO_2@CNFs$ and $MnTiO_3/TiO_2@CNFs$. It can be inferred from the figure that the MB decolorization efficiency utilizing $MnTiO_3/TiO_2@CNFs$ (82.4%) is higher than that of $TiO_2@CNFs$ (62.5%) after 120 min visible light irradiation.

3.3.1. Effect of initial dye concentration (C_i)

The effect of initial MB dye concentration on the photodegradation reaction under vis-

ible light irradiation and in the presence of $MnTiO_3/TiO_2@CNFs$ is shown in Figure 6A. It can be inferred from the figure that the MB photodegradation decreases with increasing MB concentrations due to reduced active species at higher MB concentration during the photocatalytic process [38, 39]. Also, the increase in MB concentration may cause the dye molecules to soak up light, preventing the photons from reaching the surface of the photocatalyst and thereby reducing the ef-

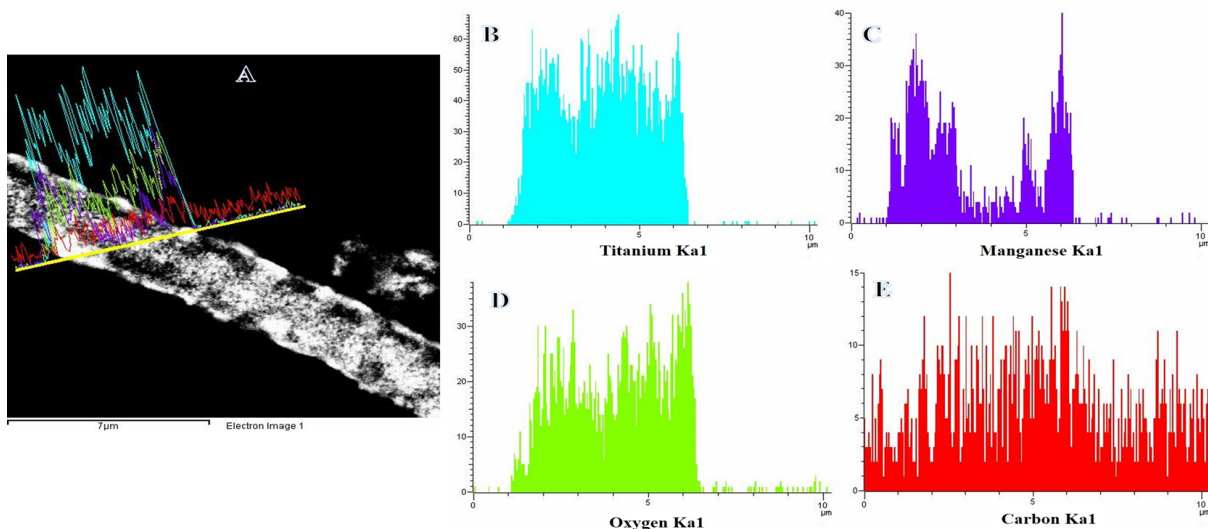


Fig. 4. (A) TEM image of a single calcined nanofiber along with the TEM EDX line analysis, (B–E) corresponding to Ti, C, O, and Mn TEM EDX line analyses. EDX, energy-dispersive X-ray spectroscopy

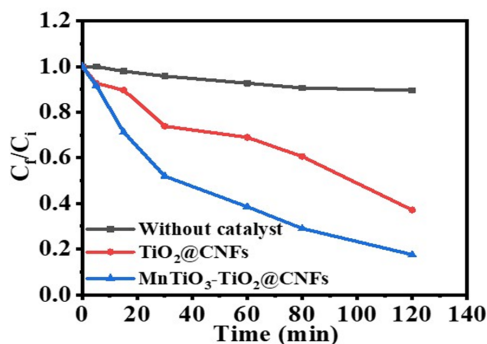


Fig. 5. The photodegradation profile of MB dye ($200 \text{ mg}\cdot\text{L}^{-1}$, $C_i = 5 \text{ mg}\cdot\text{L}^{-1}$, $T = 298 \text{ K}$, and $I = 25 \text{ W}\cdot\text{m}^{-2}$). CNFs, carbon nanofibers; MB, methylene blue

efficiency of the photodegradation process [40–42]. Thus, photodegradation process is efficient at lower MB concentrations due to the accessibility of additional active sites for MB molecules, which enhance their adsorption on the photocatalyst surface and increase their removal at low concentrations. The photodegradation of the organic compounds can be modeled via the Langmuir Hinshelwood (LH) pseudo-first order reaction according to Eq. (2).

$$r_{MB} = -\frac{dC_f}{dt} = K_1 C_f = \frac{K_{LH} K_R C_f}{1 + K_R C_i} \quad (2)$$

$$K_1 = \frac{K_{LH} K_R}{1 + K_R C_i} \quad (3)$$

Where:

r_{MB} – represents the reaction rate of MB (expressed in $\text{mg}\cdot\text{L}^{-1}\cdot\text{min}^{-1}$),

K_1 – the first order rate constant for C_i (min^{-1}),

K_{LH} – the reaction rate constant ($\text{mg}\cdot\text{L}^{-1}\cdot\text{min}^{-1}$),

t – the photocatalysis time (min),

K_R – the adsorption equilibrium constant ($\text{L}\cdot\text{mg}^{-1}$),

C_i – the initial MB dye concentration ($\text{mg}\cdot\text{L}^{-1}$),

and C_f – the final MB dye concentration ($\text{mg}\cdot\text{L}^{-1}$).

Figure 6B shows the kinetics of MB degradation in the company of various concentrations of $\text{MnTiO}_3/\text{TiO}_2$ @CNFs photocatalyst. The values of rate constant (K_1) can be obtained by the slope of straight lines obtained in Figure 6B. The value of K_1 diminishes from 0.0153 min^{-1} to 0.0044 min^{-1} as the MB concentration raises from $5 \text{ mg}\cdot\text{L}^{-1}$ to $15 \text{ mg}\cdot\text{L}^{-1}$, as shown in Table 1. The reason behind this may be the restricted formation of active species at higher MB concentrations.

The relation between K_1 and C_i is obtained by plotting $1/K_1$ vs. C_i (refer Figure 6C) and modifying the LH model by transforming Eq. (4) into a

straight-line equation ($y = ax + b$) as follows:

$$\frac{1}{K_1} = \frac{1}{K_{LH}}C_i + \frac{1}{K_{LH}K_R} \quad (4)$$

here: $a = \frac{1}{K_{LH}}$, $b = \frac{1}{K_R K_{LH}}$, $K_{LH} = 6.75 \times 10^{-2} \cdot \text{mg} \cdot \text{L}^{-1}$ and $K_R = 4.99 \text{ L} \cdot \text{mg}^{-1}$

3.3.2. Effect of reaction temperature

Figure 7A shows the variation of MB concentration vs. irradiation time at various reaction temperatures for MnTiO₃/TiO₂@CNFs photocatalyst. It can be inferred from the figure that the photodegradation of MB enlarged with the raise in the reaction temperature from 25°C to 40°C. The high temperature assists the mobility of charge carrier and interfacial charge transfer. As the reaction temperature increases, the photoelectron-hole pairs become more mobile, due to which electrons rapidly unite with the adsorbed oxygen and holes can produce OH radicals more rapidly [43–45], thus obliging the MB photodegradation process. Temperature ranging from 20°C to 80°C is considered to be the most suitable for effective photodegradation of organic compounds [43, 46]. Further increase in the reaction temperature reduces the photocatalytic activity since the electron-hole recombination rate increases [43], while low reaction temperature reduces the MB solubility in water, causing partial condensation of MB in water [43, 47]. Figure 7B shows the kinetics of the MB photodegradation given the existence of MnTiO₃/TiO₂@CNFs at various temperatures. The value of reaction rate (K_2) is increased from 0.0153 min⁻¹ to 0.0222 min⁻¹ with the increase in reaction temperature from 25°C to 40°C, as shown in Table 1. This implies an enhancement in the MB photodegradation efficiency with the temperature increase due to high charge mobility. The rate constant (K_2) can be firm, as observed from the slope of straight lines obtained in Figure 7B. The plot of K_2 vs. $1/T$ shows a straight-line relation, as shown in Figure 7C. To obtain the activation energy (E_a) of the photocatalyst, we employ the Arrhenius Eq. (5).

$$K_2 = A \exp\left(\frac{E_a}{RT}\right) \quad (5)$$

where K_2 represents the first order rate constant for T (expressed in min⁻¹) and A the frequency factor (min⁻¹).

Applying natural log to both sides of Eq. (5) yields Eq. (6), as follows:

$$\ln K_2 = \ln A + \left(\frac{E_a}{R}\right) \left(\frac{1}{T}\right) \quad (6)$$

which is a straight line curve $y = ax + b$ with $a = \frac{E_a}{R}$ and $E_a = 1.9204 \times 10^4 \text{ J} \cdot \text{mol}^{-1}$.

3.3.3. Effect of light intensity

The photodegradation rate of organic compounds relies on the wavelength and intensity of light [40, 48–50]. Figure 8A represents the influence of intensity of light on the MB photodegradation. It suggests that the rate of MB photodegradation is boosted as the intensity of light is raised. An augment in the intensity of light implies enhancement in the number of photons, due to which the MB photodegradation increases. The rate constant (K_3) can be determined from the slope of straight lines obtained from the plot of $\ln(C_i/C_f)$ against time under various light intensities, as revealed in Figure 8B. The value of K_3 is amplified from 0.0153 min⁻¹ to 0.0228 min⁻¹ with the raise in light intensity from 25 W·m⁻² to 40 W·m⁻², as shown in Table 1. This suggests an enhancement in the MB photodegradation competence with the increase in light intensity. We obtained the relation between K_3 and I by plotting $1/K_3$ vs. I (see Figure 8C) and found K_3 to be directly proportional to I [37], in the form $y = ax$, where $a = m$, $x = I$, and $m = 6 \times 10^{-4}$.

$$K_3 = mI \quad (7)$$

where K_3 represents the first order rate constant for I , and is expressed in min⁻¹.

3.3.4. Effect of MnTiO₃/TiO₂@CNFs photocatalyst dosage on MB degradation

Figure 9A shows the concentration of MB vs. irradiation time at various MnTiO₃/TiO₂@CNFs dosages. The efficiency of MB photodegradation increases with the increase in MnTiO₃/TiO₂@CNFs dosage in anticipation

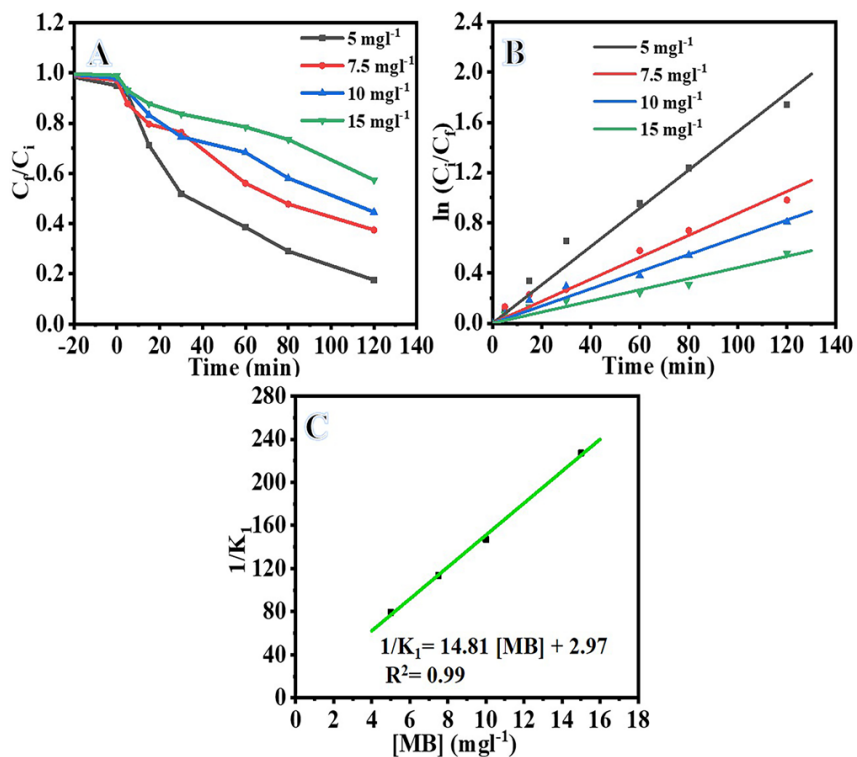


Fig. 6. (A) Effect of MB on the photodegradation of MB, (B) plot of $\ln C_i/C_f$ vs. time, and (C) modified LH plot for MB photodegradation ($200 \text{ mg}\cdot\text{L}^{-1}$, $T = 298 \text{ K}$, and $I = 25 \text{ W}\cdot\text{m}^{-2}$). LH, Langmuir Hinshelwood; MB, methylene blue

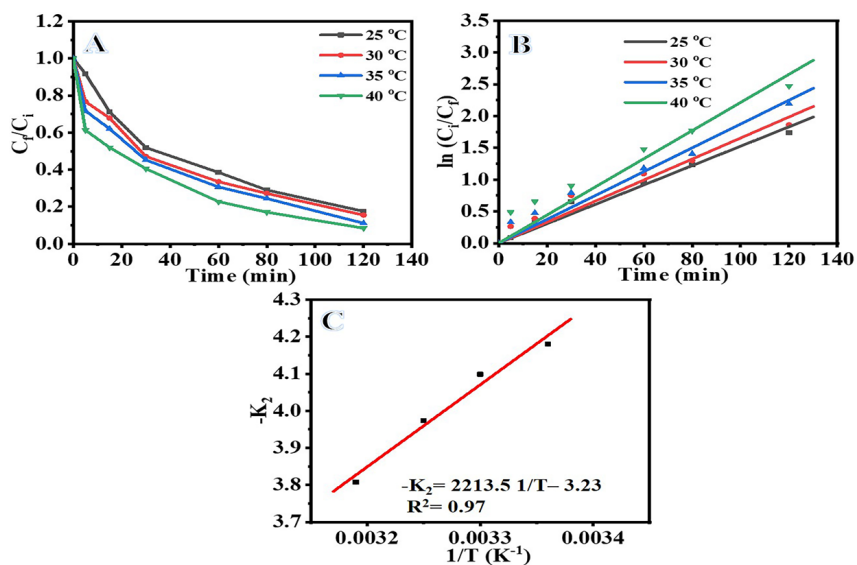


Fig. 7. (A) Effect of reaction temperature on photodegradation of MB, (B) plot of $\ln C_i/C_f$ vs. time, and (C) Arrhenius plot for MB photodegradation ($200 \text{ mg}\cdot\text{L}^{-1}$, $C_i = 5 \text{ mg}\cdot\text{L}^{-1}$, and $I = 25 \text{ W}\cdot\text{m}^{-2}$). MB, methylene blue

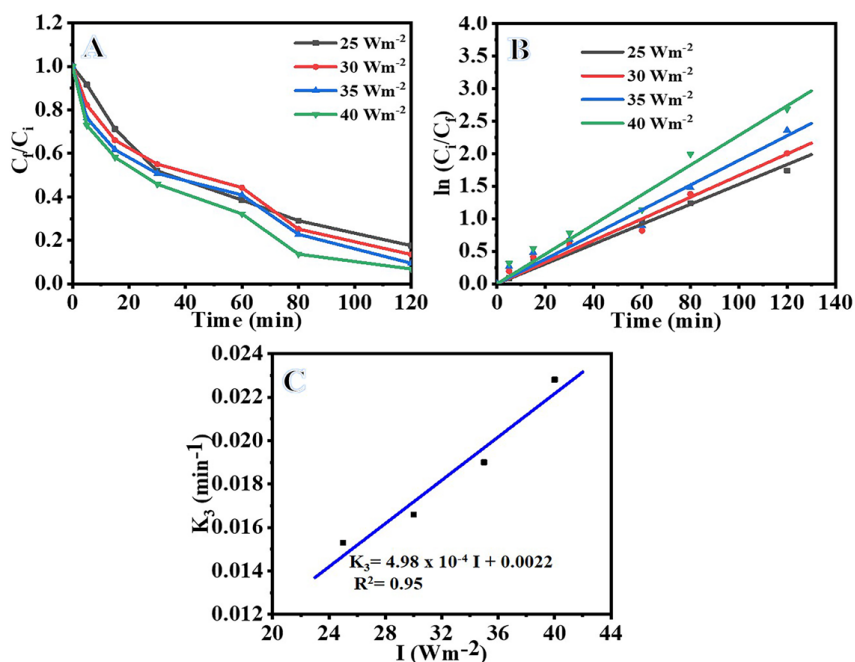


Fig. 8. (A) Effect of light intensity on photodegradation of MB, (B) plot of $\ln C_t/C_f$ vs. time, and (C) plot of K_3 vs. I ($200 \text{ mg}\cdot\text{L}^{-1}$, $C_i = 5 \text{ mg}\cdot\text{L}^{-1}$, and $T = 298 \text{ K}$). MB, methylene blue

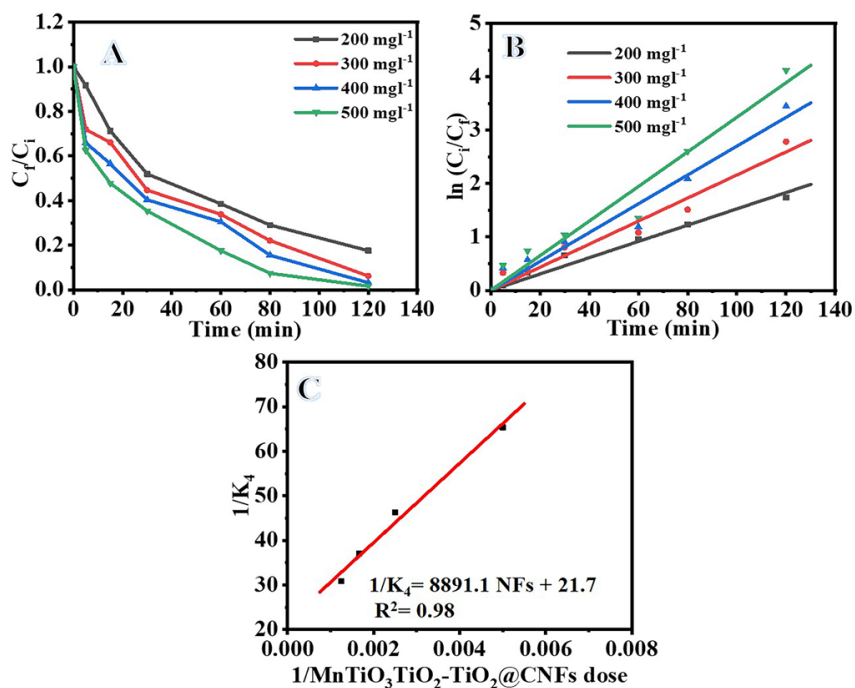


Fig. 9. (A) Effect of catalyst amount on photodegradation of MB, (B) plot of $\ln C_t/C_f$ vs. time, and (C) Langmuir-type plot for photodegradation of MB ($C_i = 5 \text{ mg}\cdot\text{L}^{-1}$, $T = 298 \text{ K}$, and $I = 25 \text{ W}\cdot\text{m}^{-2}$). CNFs, carbon nanofibers; MB, methylene blue

Table 1. Reaction rate constants of MB photodegradation at various MB concentrations, reaction temperatures, light intensities, and MnTiO₃/TiO₂@CNFs dosages

Rate constant (min ⁻¹)	MB dye concentration (C _i) (mg · L ⁻¹)
0.0153	5
0.0088	7.5
0.0068	10
0.0044	15
Rate constant (min ⁻¹)	Reaction temperature (T) (°C)
0.0153	25 T
0.0166	30
0.0188	35
0.0222	40
Rate constant (min ⁻¹)	Light intensity (I) (W · m ⁻²)
0.0153	25 I
0.0166	30
0.019	35
0.0228	40
Rate constant (min ⁻¹)	Catalyst dosage (C _{NFs}) (mg · L ⁻¹)
0.0153	200
0.0216	400
0.027	600
0.0324	800

CNFs, carbon nanofibers; MB, methylene blue

of the available active sites that improve the MB photodegradation. It is also observed that the MB photodegradation at 400 mg · L⁻¹ is very close to that at the dosage of 500 mg · L⁻¹. The reason underlying this result is reduction of the available active sites due to the aggregation phenomenon at high MnTiO₃/TiO₂@CNFs dosage. It may be also due to the light scattering and screening effect that decrease the photoreactions and active radicals [39, 51–53]. Figure 9B represents the kinetics of the MB photodegradation given the existence of MnTiO₃/TiO₂@CNFs at various catalyst dosages.

The value of the reaction constant (K₄) is increased from 0.0126 min⁻¹ to 0.0245 min⁻¹ with the increase in the photocatalyst dosage from 200 mg · L⁻¹ to 500 mg · L⁻¹, as shown in Table 1. The improvement in the MB photodegradation efficiency due to the increase in MnTiO₃/TiO₂@CNFs dosage facilitates the availability of active sites on the surface of the catalyst. The influence of the MnTiO₃/TiO₂@CNFs dosage on K₄ is determined by employing a Langmuir-type relation [37, 54] ac-

ording to Figure 9C and Eq. (8).

$$K_4 = \frac{K_0 K_{NFs} C_{NFs}}{1 + K_{NFs} C_{NFs}} \quad (8)$$

Eq. (8) can be transformed to a straight-line equation ($y = ax + b$) as shown in Eq. (9).

$$\frac{1}{K_4} = \frac{1}{K_0 K_{NFs}} \left(\frac{1}{C_{NFs}} \right) + \frac{1}{K_0} \quad (9)$$

where

K₄ represents the first order rate constant for C_{NFs} (expressed in min⁻¹),

K₀ – the reaction rate constant for C_{NFs} (min⁻¹),

$a = 1/K_0 K_{NFs}$,

$K_0 = 4.6 \times 10^{-2} \cdot \text{min}^{-1}$

and $K_{NFs} = 2.444 \times 10^{-3} \cdot \text{L} \cdot \text{mg}^{-1}$.

3.3.5. Development of reaction rate model

The aforementioned results obtained in Eqs (6), (7), and (9) suggest that the rate constant is a function of the MB concentration, light intensity, reaction temperature, and MnTiO₃/TiO₂@CNFs

dosages. The values of K_R , E_a , m , and K_{NFS} obtained from multiple regression analysis are shown in Table 2. The equation constant K' is calculated from Eq. (1) by substituting the previously obtained values of C_i , T , I , and C_{NFS} and constant values from Table 2.

$$K_{app} = K' \left(\frac{4.99}{1 + 4.99 \times 5} \right) \cdot \left(\frac{2.444 \times 10^{-3} \times 200}{1 + 2.444 \times 10^{-3} \times 200} \right) \cdot \left(\exp \frac{-1.9204 \times 10^4}{8.314 \times 298} \right) (6 \times 10^{-4} \times 25) \quad (10)$$

The reaction rate constant (K_{app}) can be rewritten as follows:

$$K_{app} = 3.7551 \times 10^4 \left(\frac{4.99}{1 + 4.99 \times C_i} \right) \cdot \left(\frac{2.444 \times 10^{-3} \times C_{NFS}}{1 + 2.444 \times 10^{-3} \times C_{NFS}} \right) \cdot \left(\exp \frac{-1.9204 \times 10^4}{8.314 \times T} \right) (6 \times 10^{-4} \times I) \quad (11)$$

A comparison between the experimental and calculated values of K_{app} for the MB photodegradation under various conditions is shown in Figure 10. The obtained plot shows that the experimental data are in good agreement with the calculated data from the model. This demonstrates that our model can successfully predict the reaction rate constant at various operational conditions.

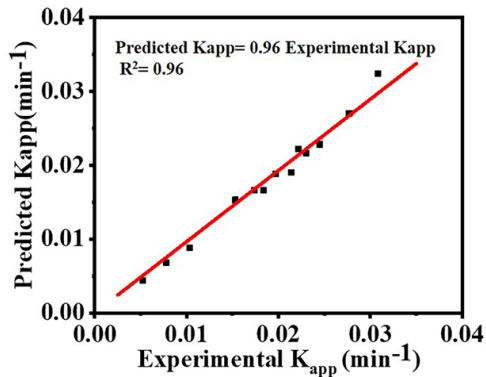


Fig. 10. Comparison between experimental and predicted K_{app} values

3.4. Photohydrolysis of H_2 from AB

The photocatalytic activity of $TiO_2@CNFs$ and $MnTiO_3/TiO_2@CNFs$ toward the H_2 release from the hydrolysis of AB (1 mmol AB) is measured under the visible light irradiation ($I = 25 \text{ W}\cdot\text{m}^{-2}$), as shown in Figure 11. The H_2 evolution over $TiO_2@CNFs$ and $MnTiO_3/TiO_2@CNFs$ for 12 min exposure is determined to be 0.35 mmol and 2.97 mmol, respectively. The higher photohydrolysis activity of $MnTiO_3/TiO_2@CNFs$ was observed than $TiO_2@CNFs$. This may be due to the fast separation of e^-/h^+ on $MnTiO_3/TiO_2@CNFs$, as compared with $TiO_2@CNFs$, which improves the efficiency of H_2 generation from AB photohydrolysis. A significant H_2 production enhancement was observed under visible light as compared to darkness. Moreover, no release of H_2 was detected in the absence of a catalyst even under visible light irradiation, which suggests that AB is quite stable in water.

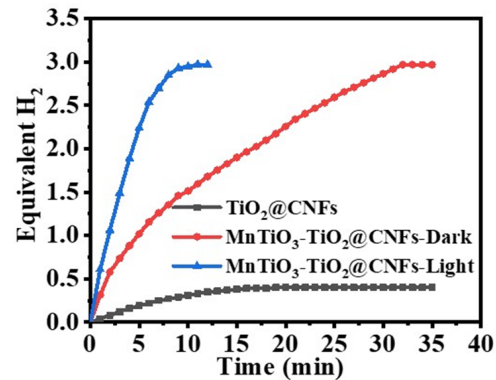


Fig. 11. H_2 generation in the presence of various photocatalysts ($200 \text{ mg}\cdot\text{L}^{-1}$, $C_i = 0.1 \text{ M}$, $T = 298 \text{ K}$, and $I = 25 \text{ W}\cdot\text{m}^{-2}$). CNFs, carbon nanofibers

3.4.1. Effect of $MnTiO_3/TiO_2@CNFs$ photocatalyst dosage on H_2 production from AB

Figure 12A shows the H_2 generation rate vs. irradiation time at various $MnTiO_3/TiO_2@CNFs$ dosages. It can be inferred from Figure 12A that the rate of H_2 production raises with the rise in $MnTiO_3/TiO_2@CNFs$ dosage. This may be owing to the enhancement of the available surface area of the $MnTiO_3/TiO_2@CNFs$, which ultimately enhances the AB photohydrolysis. Figure 12B shows

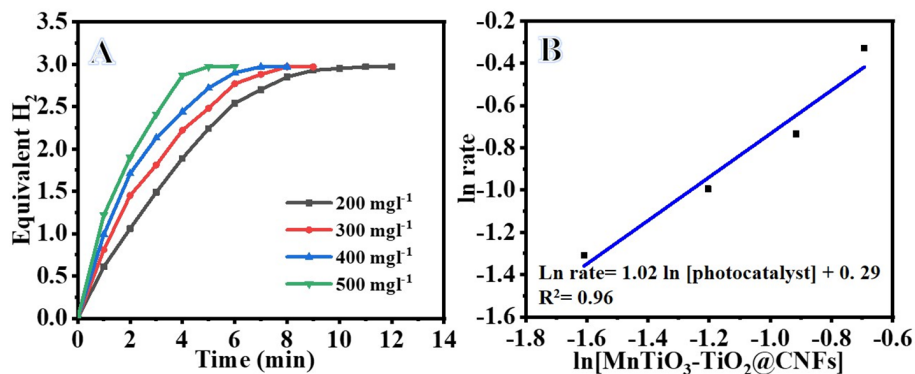


Fig. 12. (A) Effect of photocatalyst dosage on H₂ generation, and (B) plot of logarithmic value of the hydrogen production rate vs. logarithmic value of the catalyst amount ($C_i = 0.1 \text{ M}$, $T = 298 \text{ K}$, and $I = 25 \text{ W}\cdot\text{m}^{-2}$). CNFs, carbon nanofibers

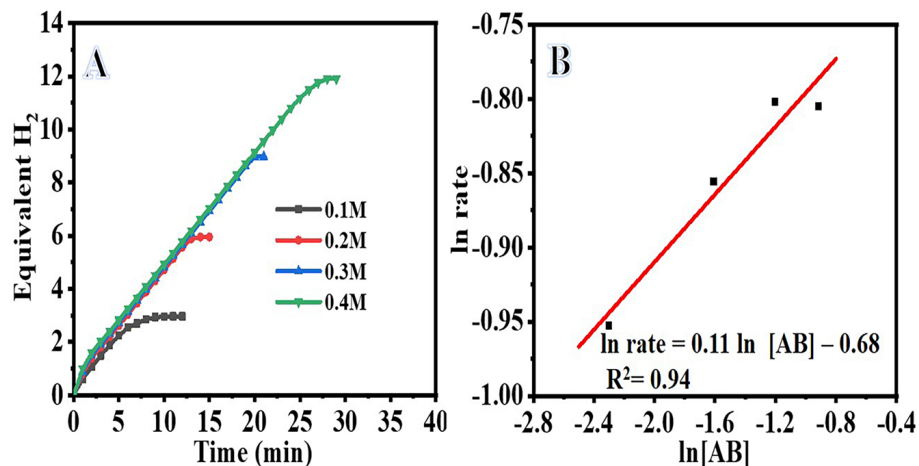


Fig. 13. (A) Effect of AB concentration on H₂ production, and (B) plot of the logarithmic value of the H₂ production rate vs. logarithmic value of the AB amount ($200 \text{ mg}\cdot\text{L}^{-1}$, $T = 298 \text{ K}$, and $I = 25 \text{ W}\cdot\text{m}^{-2}$). AB, ammonia-borane

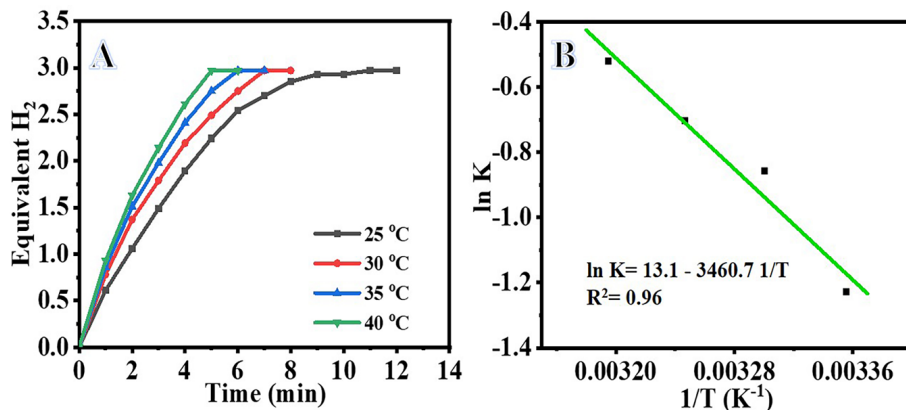
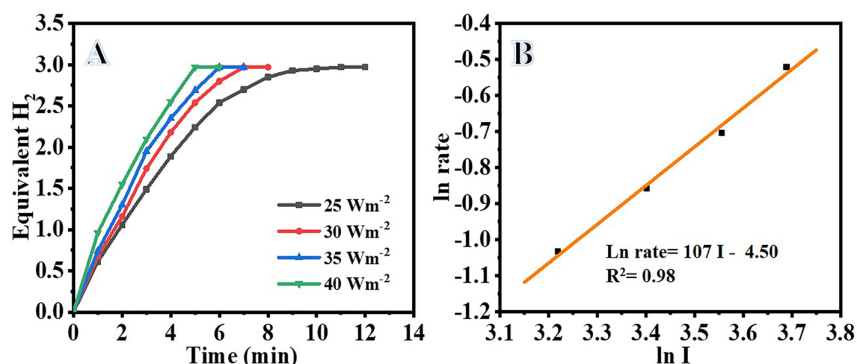


Fig. 14. (A) Effect of the reaction temperature on H₂ production, and (B) plot of logarithmic value of hydrogen production rate constant vs. $(1/T)$ ($200 \text{ mg}\cdot\text{L}^{-1}$, $C_i = 0.1 \text{ M}$, and $I = 25 \text{ W}\cdot\text{m}^{-2}$)

Table 2. Values of various constants obtained by employing multiple regression analysis in model equation

Parameter	k'	K_R (L mg ⁻¹)	E_a (J mol ⁻¹)	R (J K ⁻¹ mol ⁻¹)	m (m ² W ⁻¹ min ⁻¹)	K_{NFs} (L mg ⁻¹)
Value	3.7551×10^4	4.99	1.9204×10^4	8.314	6×10^{-4}	2.444×10^{-3}

Fig. 15. Effect of light intensity on H₂ production (A) and logarithmic value of the H₂ generation rate vs. logarithmic value of light intensity (B) (200 mg·L⁻¹, C_i = 0.1 M, and T = 298 K)

the variation of reaction rate ($\ln K$) with respect to the \ln (MnTiO₃/TiO₂@CNFs dosage). The slope of the best-fitted line is determined to be 1.028, which suggests that the generation of H₂ gas can be predicted well with the pseudo-first order kinetics in terms of catalyst dosage. The dependence of the MnTiO₃/TiO₂@CNFs dosage on K is determined by employing a Langmuir-type relation as in Eqs (11) and (12) [37, 54]. The value of K is found to be 0.361 min⁻¹.

3.4.2. Effect of initial AB concentration (C_i)

We studied the outcome of the original AB concentration on the H₂ production from AB photohydrolysis in the existence of MnTiO₃/TiO₂@CNFs upon light irradiation. Figure 13A shows that the AB concentration does not affect the H₂ generation rate, and the initial H₂ production rate almost remains unchanged even with increasing AB. The photoproduction of H₂ using various AB concentrations can be predicted via the pseudo-zero order reaction in accordance with the LH model of Eq. (3), as evidenced in Figure 13B. The incline of the best-fit line is evaluated to be 0.114, which suggests that pseudo-zero order kinetics reaction with reverence to AB was followed in H₂ production.

3.4.3. Effect of reaction temperature (T)

Figure 14A shows the H₂ production rate vs. irradiation time in the presence of MnTiO₃/TiO₂@CNFs at various reaction temperatures. As shown in the figure, the photohydrolysis of AB undergoes enhancement as the temperature increases from 25°C to 40°C. This is due to the fact that at high temperature, interfacial charge transfer and mobility of charge carrier have increased. The electron-hole pair becomes active and mobile at high temperature, where electrons combine rapidly with absorbed oxygen and holes generate OH radicals after combining with ⁻OH ions [43–45], which results in humanizing the AB photohydrolysis. The plot of K_2 vs. $1/T$ gives a straight-line relation, as shown in Figure 14B. We have observed the activation energy (E_a) as 35.36 KJ · mol⁻¹ of photocatalytic reaction via the Arrhenius Eq (8) [55].

3.4.4. Effect of light intensity (I)

The hydrogen generation rate from AB photohydrolysis is affected by the light intensity, as indicated by Figures 15A and 15B [56–58]. It is evident from the figure that the rate of AB photohydrolysis has increased concomitant with the rise in light intensity. A rise in the intensity of the light pro-

notes more photon-generation, which ultimately improves the AB photohydrolysis.

4. Mechanism of photocatalysis

The scheme of the reaction mechanism for MnTiO₃/TiO₂@CNFs catalyst is shown in Figure 16. Determining the CB and valence band (VB) potentials of the components is essential for understanding the separation of photogenerated electron-hole pairs over the MnTiO₃/TiO₂@CNFs. The following empirical formulae were used to determine these energies:

$$E_{CB} = \chi - E^e - 0.5E_g \quad (12)$$

$$E_{VB} = E_{CB} + E_g \quad (13)$$

where the VB potential is denoted by E_{VB} , and the CB potential by E_{CB} . In addition, E^e is the energy of free electrons vs. NHE, which is 4.5 eV [13, 14]. E_g is the band gap energy of the semiconductor. Finally, the electronegativity of the semiconductor is denoted by χ . In the case of TiO₂, E_g is 3.20 eV and χ is 5.81 eV, while in case of MnTiO₃, E_g is 3.10 eV and χ is 5.59 eV. The calculated E_{VB} values for MnTiO₃ and TiO₂ are 2.64 eV and 2.91 eV, respectively, vs. NHE, with corresponding E_{CB} values of -0.46 eV and -0.29 eV [13]. When compared to MnTiO₃, TiO₂ has a higher positive VB, and yet its CB is substantially more negative. Due to the adsorption capacity

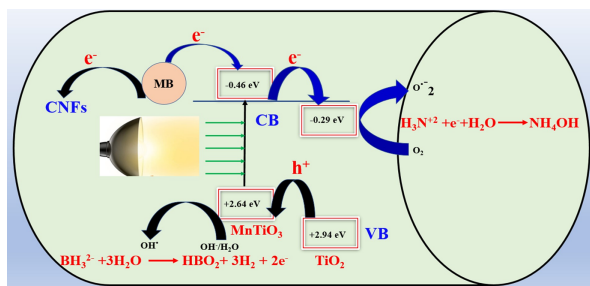
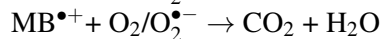
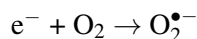


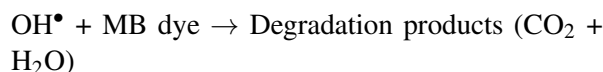
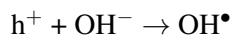
Fig. 16. Scheme for the creation and influence of electrons and holes in the photocatalytic degradation of MB and photohydrolysis of AB. AB, ammonia-borane; CB, conduction band; CNFs, carbon nanofibers; MB, methylene blue; VB, valence band

of MnTiO₃/TiO₂@CNFs, the first MB molecules were able to be adsorbed on the surface of the hybrid. When the MnTiO₃/TiO₂@CNFs and MB reaction system was illuminated with visible light, the MB dye molecules that were adsorbed on the surface of the MnTiO₃/TiO₂@CNFs were first excited and generated photoelectrons (e^-), and then the excited MB* injected electrons into the CB of MnTiO₃ [13]. Since MnTiO₃ and TiO₂ have different band gaps, injected electrons in the CB of MnTiO₃ have a tendency to move to the CB of TiO₂, which is driven by the potential energy. The redox potential has been reported to be $E_0(\text{O}_2/\text{O}_2^-) = -0.046$ eV vs. NHE) [48], which is a value that is much more positive than the CB potential of TiO₂ (-0.46 V vs. NHE). It is plausible to suppose that the $\text{O}_2^{\bullet-}$ radical species might have been readily produced by the adsorbed oxygen through the process of capturing electrons from the CB of TiO₂. As a result, the cation radical of MB was able to be effectively degraded with the assistance of the strong oxidizing power of the $\text{O}_2^{\bullet-}$. On the other hand, CNFs have the potential to operate as an electron acceptor, which not only helps to enhance the separation of electron charges, but also protects TiO₂ and MnTiO₃ nanoparticles from photocorrosion. Additionally, the VB of TiO₂ has a higher anodic energy level than the valence band (E_{VB}) of MnTiO₃. This result in holes moving from the VB of TiO₂ to the VB of MnTiO₃. As a result of the reaction of holes in the VB of MnTiO₃, OH radicals were produced. This occurred because the MnTiO₃ is more positively charged than the typical redox potentials of $\text{OH}^{\bullet}/\text{OH}$ (1.99 eV) and $\text{H}_2\text{O}^{\bullet}/\text{OH}$ (2.38 eV). Following this, the MB molecules were degraded with the assistance of the high oxidizing power of the $\text{O}_2^{\bullet-}$ and OH^{\bullet} , which may be described as follows:

In the CB—



In the VB—



5. Conclusion

We successfully prepared a heterojunction MnTiO₃/TiO₂@CNFs composite via electrospinning and calcination techniques. The synthesized composite demonstrated rapid release of hydrogen by photohydrolysis of the AB complex and the photodegradation of MB dye under visible light. We also proposed a mathematical model that successfully predicts the photocatalytic activity of composite NFs in producing H₂ via AB photohydrolysis in a batch reactor. The mathematical model effectively predicts the reaction rate constant (K_{app}) by determining the effect of various parameters employed in this study. We conclude that the experimental and theoretical data are in agreement with each other. Finally, we observe that the production of H₂ considerably increases under visible light irradiation compared to darkness.

Acknowledgements

The authors extend their appreciation to the deputyship for Research & Innovation, Ministry of Education in Saudi Arabia for funding this research work (project No. ISP20-22).

References

- [1] Houas A, Lachheb H, Ksibi M, Elaloui E, Guillard C, Herrmann JM. Photocatalytic degradation pathway of methylene blue in water. *Appl Catal B: Environ.* 2001;31:145–57.
- [2] Ràfols C, Barceló D. Determination of mono- and disulphonated azo dyes by liquid chromatography–atmospheric pressure ionization mass spectrometry. *J Chromatogr A.* 1997;777:177–92.
- [3] Han F, Kambala VSR, Srinivasan M, Rajarathnam D, Naidu R. Tailored titanium dioxide photocatalysts for the degradation of organic dyes in wastewater treatment: a review. *Appl Catal A: Gen.* 2009;359:25–40.
- [4] Chacko DK, Madhavan AA, Arun T, Thomas S, Anjusree G, Deepak T, et al. Ultrafine TiO₂ nanofibers for photocatalysis. *RSC Adv.* 2013;3:24858–62.
- [5] Reddy KR, Gomes VG, Hassan M. Carbon functionalized TiO₂ nanofibers for high efficiency photocatalysis. *Mater Res Express.* 2014;1:015012.
- [6] Reddy KR, Hassan M, Gomes VG. Hybrid nanostructures based on titanium dioxide for enhanced photocatalysis. *Appl Catal A: Gen.* 2015;489:1–16.
- [7] Nakhowong R. Fabrication and characterization of MnTiO₃ nanofibers by sol–gel assisted electrospinning. *Mater Lett.* 2015;161:468–70.
- [8] Zhou GW, Kang YS. Synthesis and structural properties of manganese titanate MnTiO₃ nanoparticle. *Mater Sci Eng: C.* 2004;24:71–4.
- [9] García-Muñoz P, Pliego G, Zazo JA, Bahamonde A, Casas JA. Ilmenite (FeTiO₃) as low cost catalyst for advanced oxidation processes. *J Environ Chem Eng.* 2016;4:542–8.
- [10] Zazo JA, García-Muñoz P, Pliego G, Silveira JE, Jaffe P, Casas JA. Selective reduction of nitrate to N₂ using ilmenite as a low cost photo-catalyst. *Appl Catal B: Environ.* 2020;273:118930.
- [11] Ghaemifar S, Rahimi-Nasrabadi M, Pourmasud S, Eghbali-Arani M, Behpour M, Sobhani-Nasab A. Preparation and characterization of MnTiO₃, FeTiO₃, and CoTiO₃ nanoparticles and investigation various applications: a review. *J Mater Sci: Mater Electron.* 2020;31:6511–24.
- [12] Song Z-Q, Wang S-B, Yang W, Li M, Wang H, Yan H. Synthesis of manganese titanate MnTiO₃ powders by a sol–gel–hydrothermal method. *Mater Sci Eng: B.* 2004;113:121–4.
- [13] Li J, Ng DHL, Kwong FL, Chiu KL. Hierarchically porous TiO₂-MnTiO₃/hollow activated carbon fibers heterojunction photocatalysts with synergistic adsorption-photocatalytic performance under visible light. *J Porous Mater.* 2017;24:1047–59.
- [14] Li X, Zhang H, Luo J, Feng Z, Huang J. Hydrothermal synthesized novel nanoporous g-C₃N₄/MnTiO₃ heterojunction with direct Z-scheme mechanism. *Electrochim Acta.* 2017;258:998–1007.
- [15] He H, Dong W, Zhang G. Photodegradation of aqueous methyl orange on MnTiO₃ powder at different initial pH. *Res Chem Intermed.* 2010;36:995–1001.
- [16] Alkaykh S, Mbarek A, Ali-Shattle EE. Photocatalytic degradation of methylene blue dye in aqueous solution by MnTiO₃ nanoparticles under sunlight irradiation. *Helvion.* 2020;6:e03663.
- [17] Bae KN, Noh SI, Ahn H-J, Seong T-Y. Effect of MnTiO₃ surface treatment on the performance of dye-sensitized solar cells. *Mater Lett.* 2013;96:67–70.
- [18] Yousef A, Brooks RM, Abutaleb A, El-Newehy MH, Al-Deyab SS, Kim HY. One-step synthesis of Co-Ti-carbon composite nanofibers at low temperature. *Ceram Int.* 2017;43:5828–31.
- [19] Yousef A, Brooks RM, El-Halwany M, Abutaleb A, El-Newehy MH, Al-Deyab SS, et al. Electrospun CoCr₇C₃-supported C nanofibers: effective, durable, and chemically stable catalyst for H₂ gas generation from ammonia borane. *Molecular Catalysis.* 2017;434:32–8.
- [20] Moradi M, Vasseghian Y, Khataee A, Harati M, Arfaeinia H. Ultrasound-assisted synthesis of FeTiO₃/GO nanocomposite for photocatalytic degradation of phenol under visible light irradiation. *Sep Purif Technol.* 2020;261:118274.
- [21] Unalan HE, Wei D, Suzuki K, Dalal S, Hiralal P, Matsumoto H, et al. Photoelectrochemical cell using dye sensitized zinc oxide nanowires grown on carbon fibers. *Appl Phys Lett.* 2008;93:133116.
- [22] Liu J, Li J, Sedhain A, Lin J, Jiang H. Structure and pho-

- toluminescence study of TiO₂ nanoneedle texture along vertically aligned carbon nanofiber arrays. *J Phys Chem C*. 2008;112:17127–32.
- [23] Yousef A, Barakat NAM, Kim HY. Electrospun Cu-doped titania nanofibers for photocatalytic hydrolysis of ammonia borane. *Appl Catal A: Gen*. 2013;467:98–106.
- [24] Yousef A, Brooks RM, El-Halwany MM, El-Newehy MH, Al-Deyab SS, Barakat NAM. Cu₀/S-doped TiO₂ nanoparticles-decorated carbon nanofibers as novel and efficient photocatalyst for hydrogen generation from ammonia borane. *Ceram Int*. 2016;42:1507–12.
- [25] Panthi G, Barakat NA, Khalil KA, Yousef A, Jeon K-S, Kim HY. Encapsulation of CoS nanoparticles in PAN electrospun nanofibers: effective and reusable catalyst for ammonia borane hydrolysis and dyes photodegradation. *Ceram Int*. 2013;39:1469–76.
- [26] Yousef A, Barakat NA, Amna T, Al-Deyab SS, Hassan MS, Abdel-Hay A, et al. Inactivation of pathogenic *Klebsiella pneumoniae* by CuO/TiO₂ nanofibers: a multifunctional nanomaterial via one-step electrospinning. *Ceram Int*. 2012;38:4525–32.
- [27] Yousef A, Barakat NA, Kim HY. Electrospun Cu-doped titania nanofibers for photocatalytic hydrolysis of ammonia borane. *Appl Catal A: Gen*. 2013;467:98–106.
- [28] Yousef A, Brooks RM, El-Halwany M, EL-Newehy MH, Al-Deyab SS, Barakat NA. Cu₀/S-doped TiO₂ nanoparticles-decorated carbon nanofibers as novel and efficient photocatalyst for hydrogen generation from ammonia borane. *Ceram Int*. 2016;42:1507–12.
- [29] Yousef A, Brooks RM, El-Halwany MM, Obaid M, El-Newehy MH, Al-Deyab SS, et al. A novel and chemical stable Co–B nanoflakes-like structure supported over titanium dioxide nanofibers used as catalyst for hydrogen generation from ammonia borane complex. *Int J Hydrog Energy*. 2016;41:285–93.
- [30] Yousef A, El-Halwany M, Barakat NA, Al-Maghrabi MN, Kim HY. Cu₀-doped TiO₂ nanofibers as potential photocatalyst and antimicrobial agent. *J Ind Eng Chem*. 2015;26:251–8.
- [31] Al-Enizi AM, Brooks RM, Abutaleb A, El-Halwany M, El-Newehy MH, Yousef A. Electrospun carbon nanofibers containing Co-TiC nanoparticles-like superficial protrusions as a catalyst for H₂ gas production from ammonia borane complex. *Ceram Int*. 2017;43:15735–42.
- [32] Al-Enizi AM, El-Halwany MM, Al-Abdrabnabi MA, Bakrey M, Ubaidullah M, Yousef A. Novel low temperature route to produce CdS/ZnO composite nanofibers as effective photocatalysts. *Catalysts*. 2020;10:417.
- [33] Al-Enizi AM, Nafady A, El-Halwany M, Brooks RM, Abutaleb A, Yousef A. Electrospun carbon nanofiber-encapsulated NiS nanoparticles as an efficient catalyst for hydrogen production from hydrolysis of sodium borohydride. *Int J Hydrog Energy*. 2019;44:21716–25.
- [34] Yousef A, Brooks RM, El-Newehy MH, Al-Deyab SS, Kim HY. Electrospun Co-TiC nanoparticles embedded on carbon nanofibers: active and chemically stable counter electrode for methanol fuel cells and dye-sensitized solar cells. *Int J Hydrog Energy*. 2017;42:10407–15.
- [35] Xue Z, Xiong Q, Zou C, Chi H, Hu X, Ji Z. Growth of carbon nanofibers through chemical vapor deposition for enhanced sodium ion storage. *Mater Res Bull*. 2021;133:111049.
- [36] Ning X, Zhong W, Li S, Wang Y, Yang W. High performance nitrogen-doped porous graphene/carbon frameworks for supercapacitors. *J Mater Chem A*. 2014;2:8859–67.
- [37] Ali I, Park S, Kim J-O. Modeling the photocatalytic reactions of g-C₃N₄-TiO₂ nanocomposites in a recirculating semi-batch reactor. *J Alloys Compd*. 2020;821:153498.
- [38] Wang R-C, Yu C-W. Phenol degradation under visible light irradiation in the continuous system of photocatalysis and sonolysis. *Ultrason Sonochem*. 2013;20:553–64.
- [39] Moradi M, Vasseghian Y, Khataee A, Harati M, Arfaeinia H. Ultrasound-assisted synthesis of FeTiO₃/GO nanocomposite for photocatalytic degradation of phenol under visible light irradiation. *Sep Purif Technol*. 2021;261:118274.
- [40] Alkaykh S, Mbarek A, Ali-Shattle EE. Photocatalytic degradation of methylene blue dye in aqueous solution by MnTiO₃ nanoparticles under sunlight irradiation. *Helvion*. 2020;6:e03663.
- [41] Mengyue Z, Shifu C, Yaowu T. Photocatalytic degradation of organophosphorus pesticides using thin films of TiO₂. *J Chem Technol Biotechnol*. 1995;64:339–44.
- [42] Ming L. Treatment of dye aqueous solution by UV/TiO₂ process with applying bias potential. *Water Sci*. 2000;36:189–06.
- [43] Chen Y-W, Hsu Y-H. Effects of reaction temperature on the photocatalytic activity of TiO₂ with Pd and Cu cocatalysts. *Catalysts*. 2021;11:966.
- [44] Meng Y, Xia S, Pan G, Xue J, Jiang J, Ni Z. Preparation and photocatalytic activity of composite metal oxides derived from Salen-Cu (II) intercalated layered double hydroxides. *Korean J Chem Eng*. 2017;34:2331–41.
- [45] Ojstršek A, Kleinschek KS, Fakin D. Characterization of nano-sized TiO₂ suspensions for functional modification of polyester fabric. *Surf Coat Technol*. 2013;226:68–74.
- [46] Kumar A, Pandey G. A review on the factors affecting the photocatalytic degradation of hazardous materials. *Mater Sci Eng Int J*. 2017;1:1–10.
- [47] Salimi A, Roosta A. Experimental solubility and thermodynamic aspects of methylene blue in different solvents. *Thermochim Acta*. 2019;675:134–9.
- [48] Ahmed S, Rasul M, Martens WN, Brown R, Hashib M. Heterogeneous photocatalytic degradation of phenols in wastewater: a review on current status and developments. *Desalination*. 2010;261:3–18.
- [49] Li Puma G, Yue PL. Effect of the radiation wavelength on the rate of photocatalytic oxidation of organic pollutants. *Ind Eng Chem Res*. 2002;41:5594–600.

- [50] Kaneco S, Rahman MA, Suzuki T, Katsumata H, Ohta K. Optimization of solar photocatalytic degradation conditions of bisphenol A in water using titanium dioxide. *J Photochem Photobiol A: Chem* 2004;163:419–24.
- [51] Giannakoudakis DA, Farahmand N, Łomot D, Sobczak K, Bandosz TJ, Colmenares JC. Ultrasound-activated TiO₂/GO-based bifunctional photoreactive adsorbents for detoxification of chemical warfare agent surrogate vapors. *Chem Eng J*. 2020;395:125099.
- [52] Fathinia M, Khataee A. Photocatalytic ozonation of phenazopyridine using TiO₂ nanoparticles coated on ceramic plates: mechanistic studies, degradation intermediates and ecotoxicological assessments. *Appl Catal A: Gen*. 2015;491:136–54.
- [53] Soltani RDC, Rezaee A, Khataee A, Safari M. Photocatalytic process by immobilized carbon black/ZnO nanocomposite for dye removal from aqueous medium: optimization by response surface methodology. *J Ind Eng Chem*. 2014;20:1861–8.
- [54] Daneshvar N, Rabbani M, Modirshahla N, Behnajady MA. Kinetic modeling of photocatalytic degradation of Acid Red 27 in UV/TiO₂ process. *J Photochem Photobiol A: Chem*. 2004;168:39–45.
- [55] Marandi R, Olya ME, Vahid B, Khosravi M, Hatami M Kinetic modeling of photocatalytic degradation of an azo dye using nano-TiO₂/polyester. *Environ Eng Sci*. 2012;29:957–63.
- [56] Wei L, Yang Y, Yu Y-N, Wang X, Liu H, Lu Y, et al. Visible-light-enhanced catalytic hydrolysis of ammonia borane using RuP₂ quantum dots supported by graphitic carbon nitride. *Int J Hydrog Energy*. 2021;46:3811–20.
- [57] Wen M, Kuwahara Y, Mori K, Zhang D, Li H, Yamashita H. Synthesis of Ce ions doped metal–organic framework for promoting catalytic H₂ production from ammonia borane under visible light irradiation. *J Mater Chem A*. 2015;3:14134–41.
- [58] Simagina V, Komova O, Ozerova A, Netskina O, Odegoova G, Kayl N, et al. TiO₂-based photocatalysts for controllable hydrogen evolution from ammonia borane. *Catalysis Today*. 2021;379:149–58.

Received 2022-06-13

Accepted 2022-10-24